




Piezoelectric and magnetoelectric evaluations on PVDF/CoFe₂O₄ based flexible nanogenerators for energy harvesting applications

Muhterem Koç¹, Çiğdem Elif Demirci Dönmez², Levent Paralı^{3,*} , Ali Sarı⁴, and Selçuk Aktürk⁵

¹Departments of Industrial Design, Kütahya Dumlupınar University, 43100 Kütahya, Turkey

²Research Laboratories Center, Muğla Sıtkı Koçman University, 48000 Muğla, Turkey

³Department of Electronics and Automation, Manisa Celal Bayar University, 45400 Manisa, Turkey

⁴Department of Electrical and Energy, Manisa Celal Bayar University, 45400 Manisa, Turkey

⁵Department of Physics, Muğla Sıtkı Koçman University, 48000 Muğla, Turkey

Received: 22 October 2021

Accepted: 17 February 2022

Published online:

5 March 2022

© The Author(s), under exclusive licence to Springer Science+Business Media, LLC, part of Springer Nature 2022

ABSTRACT

In this study, flexible PVDF/CoFe₂O₄ based nanogenerators were fabricated using composite fibers which were prepared by combining polyvinylidene difluoride (PVDF) and cobalt ferrite (CoFe₂O₄) nanoparticles (NPs: ~16 nm diameter) at a concentration of 1, 3, 5, 7, and 10 wt%. All of the flexible PVDF/CoFe₂O₄ nanofibers were characterized by X-ray powder diffraction (XRD), Fourier transform infrared spectroscopy (FTIR), and scanning electron microscopy (SEM). The incorporation of CoFe₂O₄ NPs into the PVDF leads to the formation a rich electroactive β-phase in the composite structure. The piezoelectric properties of nanogenerators indicate that the nanogenerator based on the PVDF/CoFe₂O₄ fibers containing CoFe₂O₄ NPs at a concentration of 3 wt% has a greater power efficiency of 27.2% at 20 Hz compared to that of the nanogenerator with the pure PVDF fibers at 10 Hz, under the same resistive load of 2.5 MΩ. The results also show the magnetoelectric properties of the nanogenerator with PVDF + 10 wt% CoFe₂O₄ reached the highest voltage value of 18.87mV at the same load resistive load (2.5 MΩ) for a low-level magnetic field frequency of 50 Hz. The specially improved nanogenerators which have capability of producing electrical signals at the same time from mechanical and magnetic stimulations hold promise for the development of wearable electronics devices.

Address correspondence to E-mail: levent.parali@cbu.edu.tr

1 Introduction

Researchers all over the world have investigated ways of obtaining cleaner energy sources from under-utilized resources such as sunlight, wind, industrial heat, mechanical vibrations, and magnetic fields [1–3]. Self-driven energy harvesting technologies aim to gather potential energy from the environment through induction sensors such as piezoelectric, electromagnetic, triboelectric, and electrothermal. [4]. Piezoelectric sensors generate electricity when they are exposed to vibrational stress [5] while the electromagnetic sensors harvest electricity obtained from the magnetic field through the use of power cables that have a frequency of 50–60 Hz [6–8].

Multiferroic materials can exhibit properties of ferroelectricity, ferromagnetism, ferroelasticity, and ferrotoroidicity for a single phase [9, 10]. The coexistence of at least two ferroic properties like the ferroelectric and the ferromagnetic in a magnetoelectric (ME) composite structure has attracted attention because of the potential for such devices in various areas such as sensors, transducers, multistate memory devices, switching, and filter [11–16].

ME composites obtained by combining piezoelectric and magnetostrictive materials display an ME response depending on magnetoelectric coupling interactions between the piezoelectric and magnetostrictive phases [17]. When an ME composite is placed in a magnetic environment, the magnetic field creates a strain on the magnetostrictive phase within the composite. This magnetostrictive strain is transferred to the piezoelectric phase, where it generates an electric polarization due to its piezoelectric effect [18].

In order to improve magnetoelectric coupling, several multiferroic composite architectures have been used based on different types of connectivity between ferroelectric and ferromagnetic components [19]. The 0–3 type multiferroic structure consists of a polycrystalline composite obtained with dispersed ferromagnetic particles within a ferroelectric film using methods such as the sol-gel [20], pulsed laser deposition [21], spin coating [22], solvent casting [23], or electrospinning [24]. Such structures exhibit good magnetic hysteresis (M–H) and magnetic hysteresis (P–E) loop characteristics at room temperature.

In the Simple 0–3 type ME composites, ferromagnetic particles such as NiFe_2O_4 , CoFe_2O_4 , BiFeO_3 , and Fe_3O_4 are employed as a filler in a

polyvinylidene difluoride (PVDF) polymer matrix while the PVDF is used as the ferroelectric polymer [25].

The PVDF among the electroactive polymers is a semi-crystalline polymer that exhibits five crystalline phases: α , β , γ , δ , ϵ . Since the β phase with an all-trans conformation (TTT) comprising fluorine and hydrogen atoms placed on opposite sides of the polymer chain structure exhibits net nonzero dipole moment characteristics, the β phase involving the electroactive properties of the polymer shows ferroelectric, piezoelectric, and pyroelectric properties. Hence, the importance of increasing the β phase existence among the PVDF phases depending on the processing conditions [26, 27].

Whereas the electroactive PVDF can be used as ferroelectric in an ME composite structure, in order to create its ferromagnetic properties, it is necessary to select fillers that show significant magnetic ordering around room temperature. When an ME composite is exposed to a magnetic field, its dimensions change depending on the magnetostriction coefficient of the magnetic nanoparticles (NPs) that are used as filler. Spinel CoFe_2O_4 (CFO) and NiFe_2O_4 (NFO) which have the magnetostriction coefficient $\lambda_{111} = +130 \times 10^6$ and -24.5×10^6 , respectively, have been widely used in the ME composite structures [28].

Various studies have been carried out on BaTiO_3 /magnetic nanoparticle composites. For example, Slimani et al. reached some results such as decreasing the BaTiO_3 's average crystallites size, increasing the connectivity between grains, and enhancing of the BaTiO_3 material's magnetic properties and dielectric response by increasing the ratios of the magnetic spinel ferrites CNNFO, and SrCaMg in the two-phase nanocomposites ($\text{BaTiO}_3/\text{Co}_{0.5}\text{Ni}_{0.5}\text{Nb}_{0.06}\text{Fe}_{1.94}\text{O}_4$ (CNNFO) [29] and $\text{BaTiO}_3/\text{SrCaMg}$ [30]), respectively. Furthermore, Chen et al. demonstrated the feasibility of the distribution control of an electric field produced magnetoelectrically by increasing the ME coupling effect on the 2–2 type ME thin film based on the $\text{BaTiO}_3/\text{CoFe}_2\text{O}_4$ using COMSOL simulation [31]. Ciomaga et al. investigated the properties of Di-phase $\text{BaTiO}_3/\text{CoZnFe}_2\text{O}_4$ ceramic composites with randomly mixed phases which had been obtained by conventional and Spark Plasma sintering. They concluded that the grain sizes of the two types of ceramics had an impact on their functional properties, and although the magnetic

properties of the composites were very similar for the two types of ceramics, samples that were sintered with the Spark Plasma method were much stronger than their field-dependent permittivity behavior in magnetic remanence conditions [32]. Furthermore, in another study, they comparatively analyzed two types of BaTiO₃/CoFe₂O₄ magnetoelectric ceramic composites with the same composition having randomly mixed phases and tri-layered structures which were consolidated to compact high density ceramics by the Spark Plasma Sintering. They deduced that although the dielectric constant of the BaTiO₃/CoFe₂O₄ magnetoelectric ceramic composites with randomly mixed phases were estimated to be almost ten times higher than by using the finite element method, the tri-layer BaTiO₃/CoFe₂O₄ composites exhibited much higher polarization values that were almost ten times higher than in the randomly mixed composites [33].

Although the literature contains some electrospun ME composite studies based on the PVDF by the addition of ferrite NPs such as NiFe₂O₄, CoFe₂O₄, Fe₃O₄, and NiZnFe₂O₄ [17, 34–36], the injection of magnetic NPs in a polymer matrix through the electrospinning method has rarely been reported to date. Furthermore, researchers have focused more on the ME composite production methods, their structural analyses, and basic electrical characteristics. Therefore, detailed electrical studies are still necessary when it comes to the connection of nanogenerator devices to an operational amplifier in the electronic system.

In this work, firstly, we prepared pure PVDF and PVDF/CFO mats (with doped weight rates of 1, 3, 5, 7, and 10 wt% of CoFe₂O₄) using the electrospinning method. After that, the flexible nanogenerators were obtained by embedding the PVDF and PVDF/CFO mats between two conductive aluminum electrodes. Morphological, structural, ferromagnetic, ferroelectric, piezoelectric, and magnetoelectric properties were investigated for determining the CoFe₂O₄ NPs effect on the nanogenerators.

2 Experimental section

2.1 Materials

PVDF (Alfa Aesar, Inc.) was used as a polymer material. N-Dimethylformamide (Merck, 99.5%), and

acetone (Merck, 96%) were used as solvents for the preparation of the polymer solution. To synthesize the CoFe₂O₄ nanoparticles, Iron (III) chloride hexahydrate (FeCl₃·6H₂O), (Merck, 99%), Cobalt (II) chloride hexahydrate (CoCl₂·6H₂O), (Merck, 98.0%), and sodium hydroxide (NaOH), (Tekkim, ≥ 98.0%) were used as starting materials. Oleic acid (Sigma-Aldrich, technical grade, 90%) and ultra-pure water (Type I) were used as a surfactant and solvent, respectively. The chemicals were used as received. No further purification was done.

2.2 Synthesis of cobalt ferrite (CoFe₂O₄) nanoparticles

The CoFe₂O₄ nanoparticles were synthesized by the coprecipitation method [37]. Oleic acid, iron (III) chloride hexahydrate, cobalt (II) chloride hexahydrate, and sodium hydroxide were used as surfactant and precipitating agents, respectively. First, aqueous solutions of 0.4 M of iron (III) chloride hexahydrate (65 ml) and 0.2 M of cobalt (II) chloride hexahydrate (65 ml) were prepared. Ultra-pure water was used as a solvent. Then the aqueous solutions of precursors were mixed together and stirred at room temperature for 30 min. An aqueous solution of 3 M of sodium hydroxide (65 ml) was added to the mixed solution dropwise until a pH level of 11 was read on a pH meter. Oleic acid (250 μL) was then added drop by drop to the solution. The final solution was heated to 80 °C and maintained at this temperature for 1 h under vigorous stirring. At the end of heating, the solution was cooled down to room temperature by removing the magnetic stirrer-heater device. The magnetic nanoparticles were settled by placing the beaker containing the final solution on a magnet overnight. The collected magnetic nanoparticles from the supernatant liquid were washed twice with ultra-pure water and then once with ethanol. The washed nanoparticles were isolated from the last washing solution by centrifuging at 3000 rpm for 15 min. The dried material (at 60 °C for 24 h) was then ground into a fine powder using an agate mortar. Finally, the obtained powder of nanoparticles was annealed at 600 °C for 10 h under atmospheric pressure.

2.3 Preparation of the PVDF/CoFe₂O₄ nanofiber

PVDF nanofibers containing CoFe₂O₄ NPs were prepared by the electrospinning method with a drum

collector. The schematic preparation of the PVDF/CoFe₂O₄ mats is indicated as detailed in Fig. 1. Firstly, to obtain the composite nanofibers, the DMF and Acetone solutions were mixed in the beaker. CoFe₂O₄ NPs varying in size from 1, 3, 5, 7 to 10 wt% were first dissolved into 5 sets of a mixture of DMF: Acetone (3:7) and then dispersed in the ultrasonic disperser for 1 h. After that, 10% w/v. PVDF powder was inserted to each of the prepared solutions, and they were mixed with a stirrer for an additional 24 h at 50 °C.

Each of the pure PVDF and the PVDF/CoFe₂O₄ solutions were put into 10 mL syringes connected with a metallic needle diameter of 0.4 mm. The mentioned syringe with the solution was fixed vertically on the syringe pump. The electrospinning method was used to form fibrous composites through a typical laboratory setup mentioned in our previous study [38]. Its positive pole was applied to the metal needle while the negative end of the DC (Direct Current) high voltage source was attached to the drum collector. During the electrospinning process, the feed rate of the syringe pump was 2.0 mL/h, the distance from the drum collector to the metallic needle was 15 cm (the rotation speed of the drum

collector was 2300r/min), and the applied high voltage value was 15 kV. In this study, in order to create the aligned electrospun fibers, the rotating drum collector was selected as the collector type due to the fact that the β phase content of the PVDF is increased noticeably [39]. After the electrospinning process, the pure PVDF and the PVDF/CFO based flexible mats with various concentrations of CoFe₂O₄ (1, 3, 5, 7, and 10 wt%) were assigned as PVDF-H0, PVDF-1 C, PVDF-3 C, PVDF-5 C, PVDF-7 C, and PVDF-10 C, respectively.

2.4 Characterization techniques

The room temperature XRD patterns of the CoFe₂O₄ NPs were collected under CuK radiation (1.5418 Å) by using a Rigaku SmartLab diffractometer. The scan range of 2θ was between 10 and 100° with 1s/step scan time and 0.02° scan step size. The XRD pattern of the CoFe₂O₄ NPs was analyzed using the Rietveld refinement technique with the FullProf programme [40, 41]. The room temperature XRD patterns of the β -PVDF (Host) and the PVDF/CoFe₂O₄ composites were also collected under CuK radiation (1.5418 Å) using a PANalytical Empyrean high-resolution X-ray diffractometer. The measurement range of 10°–70°

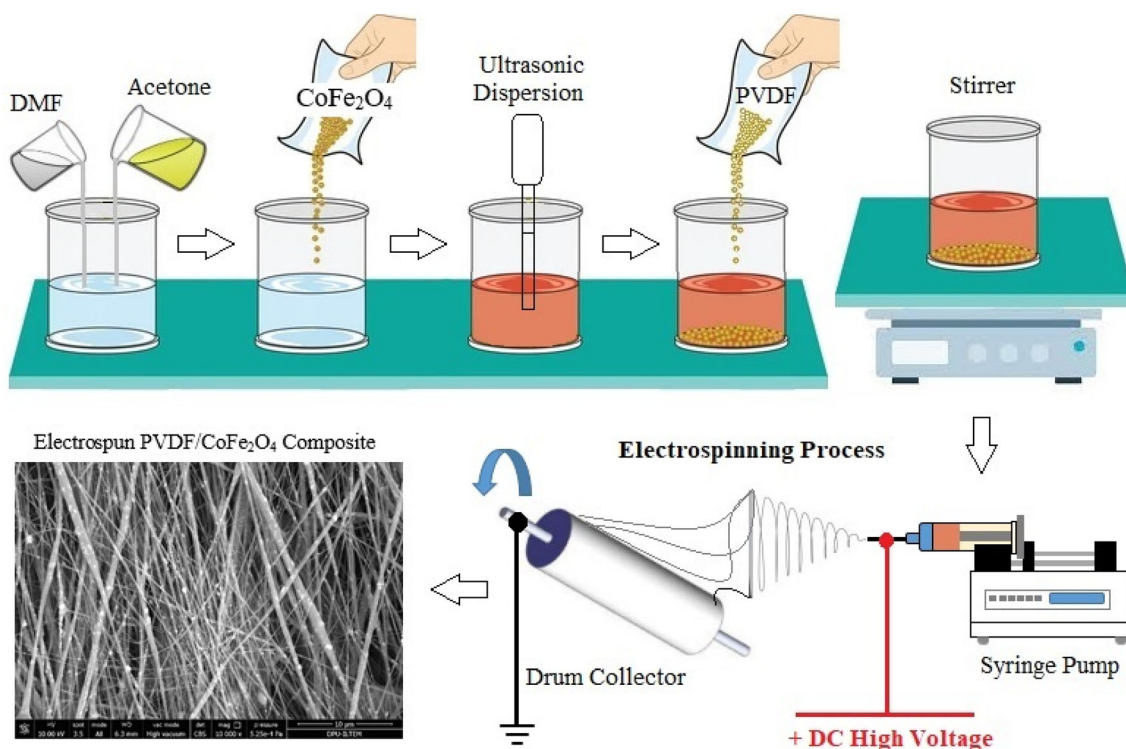


Fig. 1 Schematic preparation process of the PVDF/CFO composites

(2 θ) was scanned with a scan step size of 0.026°. The microstructure of the samples was identified using a SUPRA 40VP scanning electron microscope (SEM). The FTIR spectra were collected at room temperature for all the samples through the use of a Bruker FTIR-ATR system.

3 Results and discussion

3.1 Structural properties of the PVDF/CoFe₂O₄ nanocomposites

The XRD patterns of COF NPs, electrospun mats of pure PVDF, and PVDF/CFO composites with different weight percentages of the CoFe₂O₄ are indicated in Fig. 2a. The XRD composite mats have the typical diffraction peaks of 35.4° (311), 43.1° (400), 58.8° (511), and 62.9° (440) planes (Fig. 2b), indicating the highly crystalline cubic spinel structure of the CoFe₂O₄ NPs which is confirmed with the JCPDS (card no. 22-1086) [42]. The crystal structure of the CoFe₂O₄ NPs is defined by the cubic Fd-3 m space group with lattice parameters of 8.397 ± 0.001 Å. Scherrer broadening [43] of the diffraction peaks incorporated into the refinement provides an estimated crystalline diameter of 16.0 ± 0.2 nm for the CoFe₂O₄ NPs. No impurity was observed in the patterns.

As seen in Fig. 2a, the peak at 18.3° corresponds to the α -phase while the peak at 20.3° is associated with the β -phase of the PVDF[44–46].

It is observed from Fig. 2a that the addition of the CoFe₂O₄ NPs in the PVDF matrix gradually increases its own peak intensity in the fiber composite structure, and also the intensity of this peak enhances the interfacial interactions between the PVDF matrix and the CoFe₂O₄ NPs. The PVDF-5 C among the PVDF/CFO composites reached a peak intensity of 2 θ = 20.4° associated with the beta phase.

The infrared transmission spectra of the pure PVDF and the composite mats are shown in Fig. 3. The fraction of the β phase-F(β) can be calculated using the following equation [47]:

$$\%F(\beta) = \frac{X_{\beta}}{X_{\alpha} + X_{\beta}} = \frac{A_{\beta}}{\left(\frac{K_{\beta}}{K_{\alpha}}\right) \cdot A_{\alpha} + A_{\beta}} \times 100 \quad (1)$$

where X_{α} and X_{β} indicate the mass fractions of the α , and β phases, respectively. The A_{α} and A_{β} indicate the absorption coefficients at a particular wavenumber,

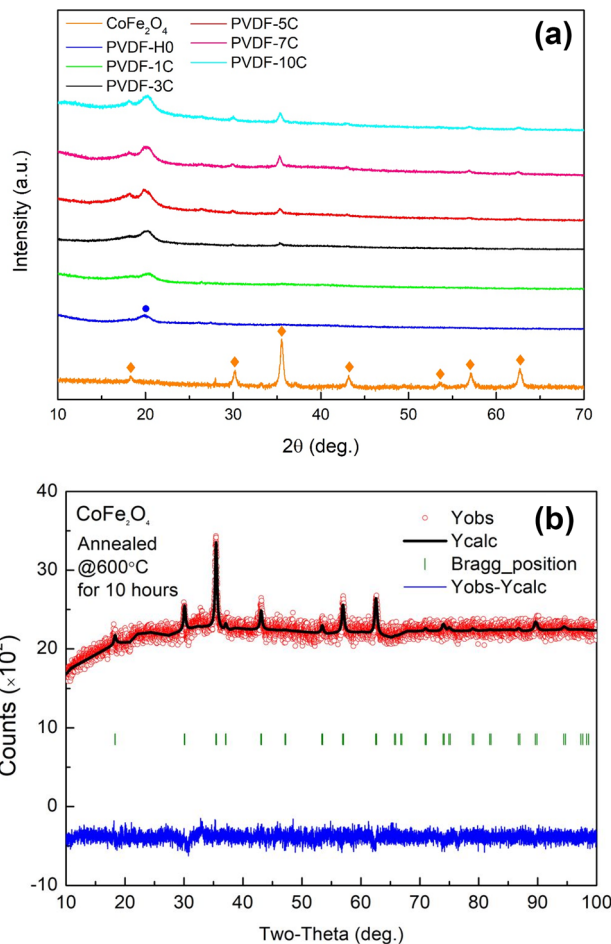


Fig. 2 XRD patterns of **a** the CoFe₂O₄ NPs (brown colored diamond—CoFe₂O₄), the pure PVDF (PVDF-H0: blue colored circle— β -PVDF) and PVDF/CFO composite mats with different weight percentages of the CoFe₂O₄ nanoparticles (PVDF-1 C, PVDF-3 C, PVDF-5 C, PVDF-7 C, and PVDF-10 C), **(b)** with the results of Rietveld refinements (black lines). The Bragg markers identify the reflections (green) and the residuals to the refinement are presented below (blue lines) (Color figure online)

which are expressed by $K_{\alpha} = 6.1 \times 10^4$ cm²/mol and $K_{\beta} = 7.7 \times 10^4$ cm²/mol, respectively [47].

As seen in Fig. 3, the FTIR spectra for the β -PVDF and the PVDF/CoFe₂O₄ nanofibers exhibit characteristic transmission peaks at bands of 478 [48], 839 [49, 50], 876 [51], 1067 [52, 53], 1169 [54], 1270 [55, 56], and 1401 [57, 58] cm⁻¹, which are assigned to the piezoelectric crystalline- β -phase while the α -phase is observed at 762 cm⁻¹ [45]. The aligned pure PVDF and PVDF/CFO fibers were observed to have a rich β -phase content. The FTIR test results are in agreement with the XRD test results.

Fig. 3 FTIR spectra of the pure PVDF, and the PVDF/ CFO composite mats with different the CoFe_2O_4 loading

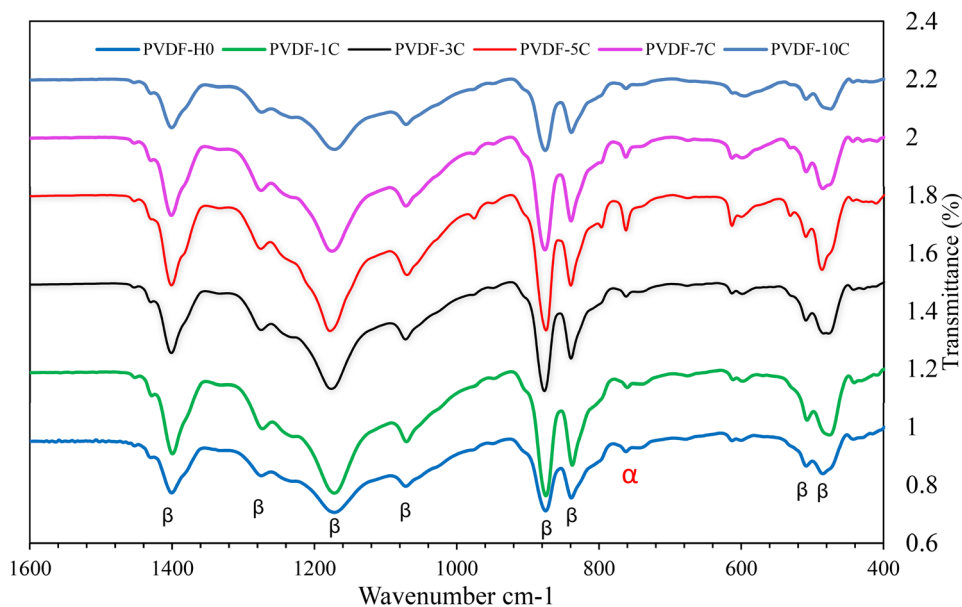


Figure 3 shows that the addition of the CoFe_2O_4 NPs in the PVDF matrix increases the peak intensity of the crystalline β -phase in the PVDF/CFO composite structure. Since the PVDF-5 C among the PVDF/CFO composites has the highest intensity peak than that of the others, a 5 wt% may be a critical concentration ratio.

3.2 Morphology analysis of the PVDF/ CoFe_2O_4 nanocomposites

The SEM images of all samples are indicated in Fig. 4. According to Fig. 4b–f, the accumulations of COF NPs are observed (marked as white spot inside a cyan-blue circle) between the PVDF/CFO fibers. This is due to the driving force of the induced electric charge, which formed on the PVDF during the electrospinning process. The thickness of the layer of the pure PVDF fiber was found to be around 63 μm by analyzing the SEM image as seen in Fig. 4 g.

According to the SEM images, the changes in the fiber diameters of the pure PVDF, and the PVDF/CFO samples depending on dopant rates are shown in Fig. 5. It was found that the pure PVDF has an average diameter of 912 nm, whereas the PVDF/CFO fibers containing the CoFe_2O_4 NPs at concentrations of 1, 3, 5, 7, and 10 wt% have average diameters of 500, 272, 223, 183, and 180 nm, respectively.

The decrease in the fiber diameters upon the addition of the CoFe_2O_4 NPs into the PVDF is in good agreement with the enhancement of crystallinity, and

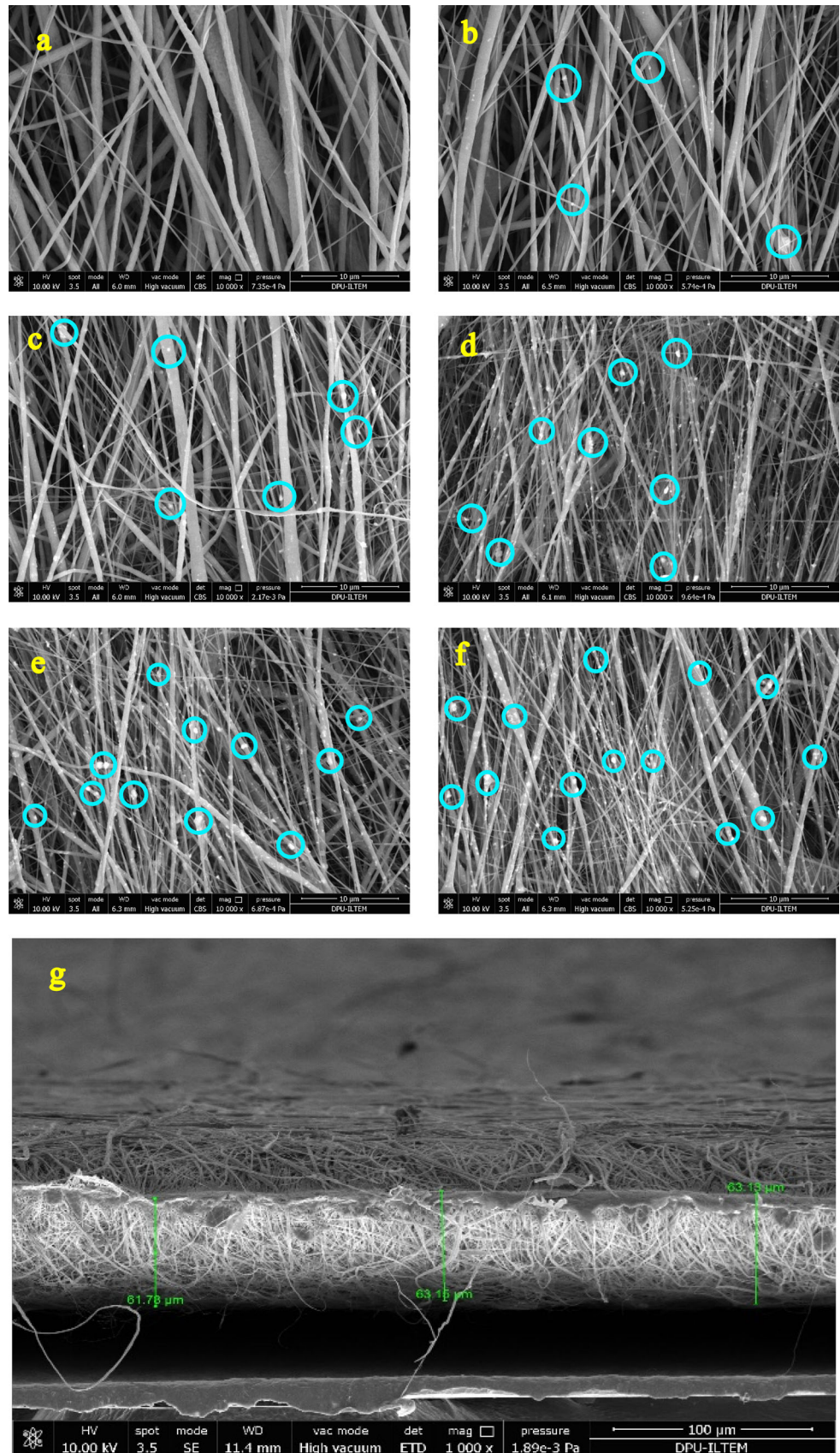
can be attributed to various factors such as viscosity, concentration, and conductivity of the polymer solution. The electrospinning parameters of the aforementioned system were optimized as explained under Sect. 2.3, since the increased filler concentration changes the solution concentration (it was 10 wt% for the pure PVDF), the viscoelastic behavior, and the charge density carried by the solution jet. This situation leads to a decrease in the PVDF/CFO fibers diameters [59, 60].

Energy dispersive X-ray (EDX) spectra, chemical compositions, and elemental mappings performed for the PVDF-10 C are indicated in detail in Fig. 6. These spectra confirm the presence of different elements such as F, C, Fe, Co, and O. The distribution of the different chemical elements was also observed via EDS elemental mappings.

3.3 The ferroelectric hysteresis loops of the PVDF/ CoFe_2O_4 nanocomposites

The electric-field-induced polarization (P-E) of the pure PVDF and the PVDF/CFO nanofiber composites that were prepared with different levels of the CoFe_2O_4 content was measured at room temperature with a maximum electrical field of 40 kV/cm, and a frequency of 1 Hz using a Precision Multiferroic II Ferroelectric Tester. The variations in the loop are shown in Fig. 7.

Fig. 4 The SEM images of the pure PVDF, and the PVDF/CFO samples with different the CoFe_2O_4 content: **a** PVDF-H0, **b** PVDF-1 C, **c** PVDF-3 C, **d** PVDF-5 C, **e** PVDF-7 C, **f** PVDF-10 C, and **g** the cross section of the pure PVDF



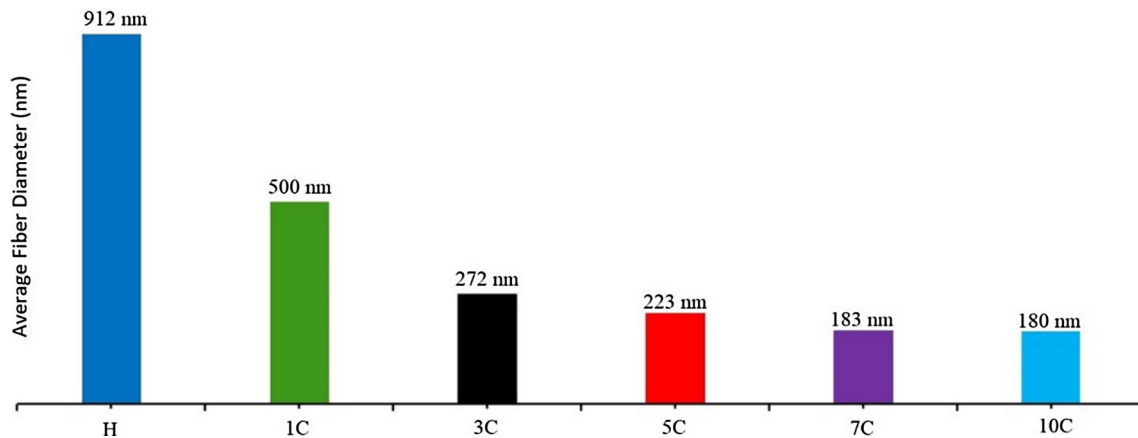


Fig. 5 The changes in the fiber diameters of the pure PVDF and the PVDF/CFO samples according to dopant rates

The P-E loops reveal that the polarization value increases with the incorporation of the CoFe_2O_4 NPs. Compared to the pure PVDF, the maximum saturation polarization (P_s) of samples reaches a value of $0.0125 \mu\text{Ccm}^{-2}$ for the PVDF/COF fibers containing the CoFe_2O_4 NPs at concentration of a 10 wt% while the least increase on P_s was observed as $0.0060 \mu\text{Ccm}^{-2}$ at a 7 wt% concentration level. Among all the samples, the PVDF/CFO nanofiber composite with the CoFe_2O_4 NPs concentration of 10 wt% exhibits the maximum saturation polarization value. Thus, it may be acknowledged as the best ferroelectric nanofiber composite.

3.4 Magnetic properties of the PVDF/ CoFe_2O_4 nanocomposites

The magnetic properties of the CoFe_2O_4 NPs and the PVDF/COF fibers were evaluated by analyzing the field-dependent magnetization (M_H) curves of the samples. M-H measurements were done at room temperature (~ 300 K) under ± 20 kOe applied fields. The room temperature magnetic hysteresis loops of the CoFe_2O_4 NPs and the PVDF /COF fibers are shown in Fig. 8a, b, respectively.

The appearance of small coercivity ($H_c \cong 610$ Oe) and small remnant magnetization ($M_r \cong 16$ emu/g) confirms the ferromagnetic nature of the CoFe_2O_4 NPs with a saturation magnetization ($M_s \cong 46$ emu/g) which is lower than the bulk CoFe_2O_4 ($M_s \cong 80$ emu/g) [24]. The lower magnetization compared to bulk can be attributed to surface disorder on the nanoparticles as a result of the finite-size effect. At very small dimensions of nanoparticles with a high surface to volume ratio, the spin disorder on the

surface, which leads to non-collinear magnetic arrangement, causes a decrease of the magnetic saturation [61]. As seen from Fig. 8b, a similar coercivity behavior to the CoFe_2O_4 NPs has been observed for the PVDF/COF fibers which confirms the ferromagnetic nature of the fibers, while a diamagnetic behavior has been observed for the pure PVDF fibers. A similar coercivity of ~ 1 kOe observed for all the PVDF/COF fibers indicated that the fibers have a coercivity which is independent from the concentration of the CoFe_2O_4 NPs in the PVDF. The saturation magnetization values of the PVDF/ CoFe_2O_4 fibers increase from 1.31 to 5.06 emu/g with the increase of the concentration of the CoFe_2O_4 NPs in the PVDF. A linearity with an R^2 value of 0.96 increased its saturation magnetization along with the increase in the concentration of the CoFe_2O_4 in the PVDF is seen in the inset in Fig. 8b. The lower magnetization of the PVDF/ CoFe_2O_4 fibers compared to the CoFe_2O_4 NPs is attributed to the presence of the non-magnetic organic component of the PVDF in the composite material, which leads to a reduction in the total magnetization, as expected. The presence of remnant magnetization and coercivity indicates that there is some amount of blocked particles in the samples of the CoFe_2O_4 NPs and the PVDF/ CoFe_2O_4 fibers which reach a high blocking temperature above 300 K [62]. This result confirms the presence of the agglomeration of the nanoparticles, which is in good agreement with those shown in the SEM images. The increase in the mean particle size of the fibers due to the agglomeration of the magnetic nanoparticles likely hinders the transition of nanoparticles from a ferromagnetic to a superparamagnetic state.

3.5 Fabrication of a flexible nanogenerator

In order to fabricate flexible nanogenerators, the pure PVDF, and the PVDF/CFO composite mats with different levels of the CoFe_2O_4 content were placed as a dielectric material between aluminum electrodes, and electric cables were attached on both sides of the electrode using silver glue. In order to preserve the flexibility of the nanogenerator with in a sandwich structure, all samples were fully covered by a thin Kapton tape. The fabrication steps of the nanogenerator, its actual photo and the schematic representation of the piezoelectric energy harvesting system are indicated in Fig. 9a–c, respectively.

The nanogenerators have the capability to act in conformity with the human body due to their own flexible structure. The movement of the nanogenerator in up-down directions creates a stretch state. At this stage, tensile and compressive stresses occurred on the upper and lower surfaces of the flexible nanogenerator. Tensile and compressive stresses changed depending on the time-dependent variable and created a continuous bidirectional movement of electrons, and this situation led to an electric pulse at alternative waveforms between the electrodes.

3.6 Dielectric Properties of flexible nanogenerator

The dielectric constant (ϵ') and the dielectric loss (ϵ'') variations of the pure PVDF and PVDF/CFO composites are exhibited in Fig. 10. It was found that the dielectric constant in the frequency range from 10 kHz to 1 MHz is almost 1.98 times higher for the PVDF/CFO fibers containing the CoFe_2O_4 NPs at 5 and 10 wt% compared to the pure PVDF fibers. The dielectric losses of the pure PVDF and the PVDF/CFO composites are related to the dielectric constant associated with the frequency, and the resulting dielectric loss values are lower.

The dielectric constant variations of the PVDF/CFO fibers containing the CoFe_2O_4 NPs at concentrations of 1, 3, 5, 7, and 10 wt% (see Fig. 10) are compatible with the polarization changes at 1 Hz for the same samples (see Fig. 7).

The ϵ' value of a dielectric material which is known as capacitance can be associated with the electrical charge and the storage capability of a nanogenerator. The induced charge on the electrode's surface increases with the increase in the PVDF/CFO

composites' dielectric constant values, which boosts the energy output of the nanogenerator [63, 64].

3.7 Energy harvesting performances of flexible nanogenerator

3.7.1 Piezoelectric effects on flexible nanogenerator

Piezoelectric energy harvesting aims to generate electricity in order to powering portable electronics devices with low power from micro- to milliwatts in response to various vibrational sources. Piezoelectric nanogenerators have the ability to directly convert changes in motion into electrical signals without any further external energy source [65]. Therefore, piezoelectric energy harvesting systems are widely used to determine the electrical energy obtained from piezoelectric nanogenerator through vibrational effects.

Figure 9c shows the experimental setup used in the piezoelectric energy harvesting system which consists of an aluminum cantilever beam and a magnetic shaker which is controlled by both a frequency generator and a power amplifier to adjust the vibrational frequency and to increase the signal amplitude at the set frequency.

This aim of this study is to determine the maximum output signals that the PVDF/CFO based nanogenerators exhibit under resistive loads, and also without resistive load. A data logger (National Instrument-6009) was used to measure the nanogenerators' open-circuit voltages (V_{oc}) as peak to peak (V_{pp}) according to various frequency values such as 5, 10, 15, 20, and 25 Hz. All obtained data were indicated on the front panel using NI LabView™ Software. The V_{oc} outputs without resistive load against the time domain of the pure PVDF and the PVDF/CFO based nanogenerators are shown in detail in Fig. 11.

The root mean square values of the voltages (V_{RMS}) were calculated by using the following equation [66]:

$$V_{RMS} = \sqrt{\frac{1}{T} \cdot \int_0^T V_{oc}(t)^2 dt} \quad (2)$$

where V_{RMS} , V_{oc} , and T indicate the effective voltage of nanogenerators, the open-circuit voltage generated from nanogenerators, and the periodic time, respectively.

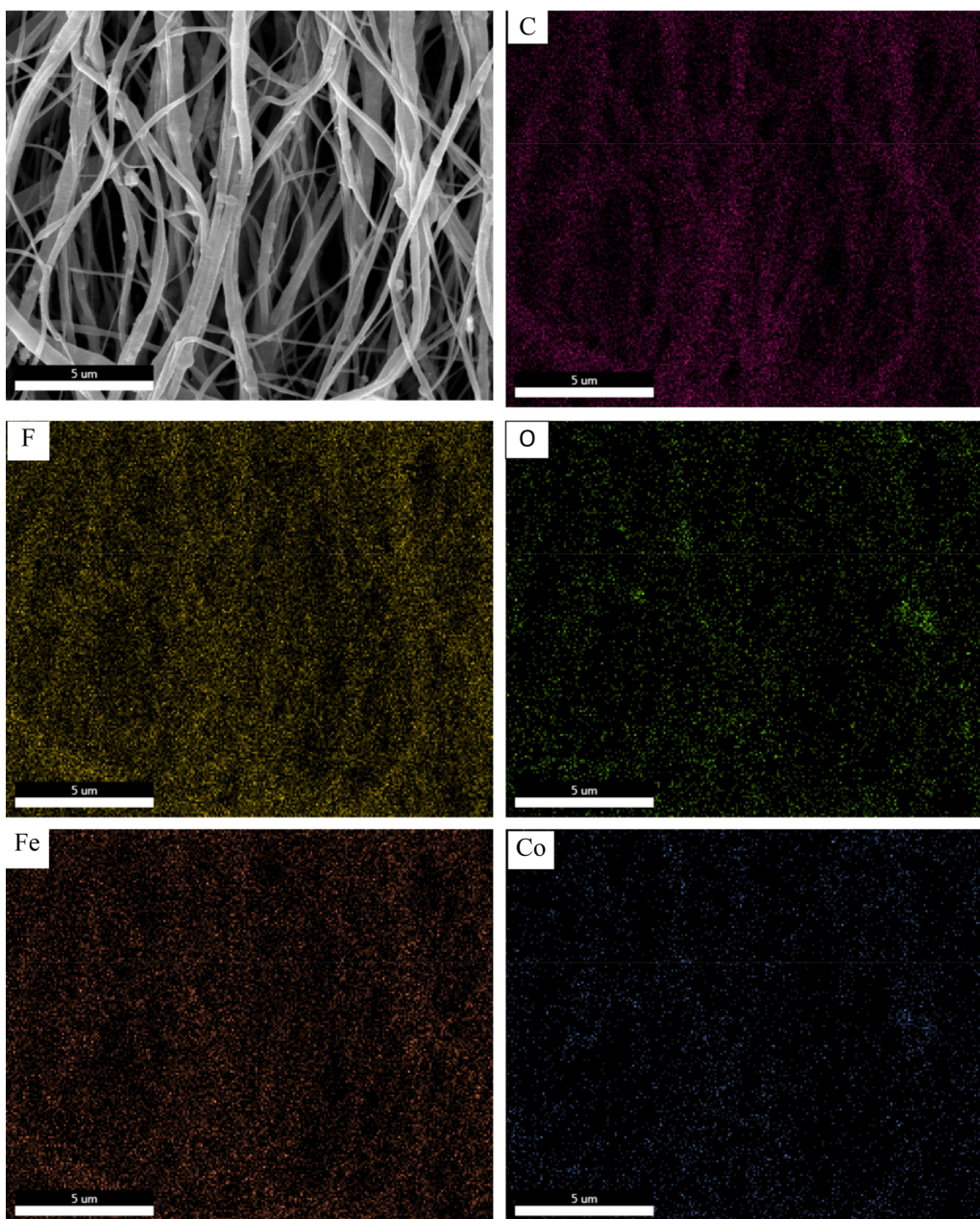
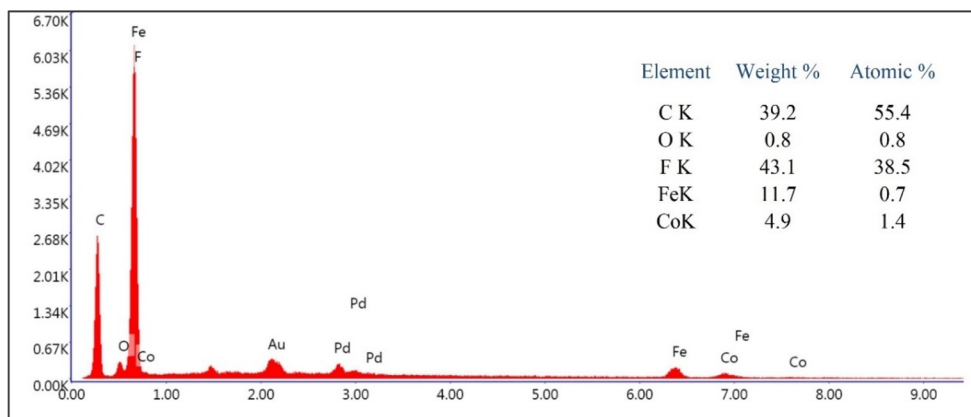


Fig. 6 Energy dispersive X-ray (EDX) spectra, chemical compositions, and elemental mapping performed for the PVDF-10 C

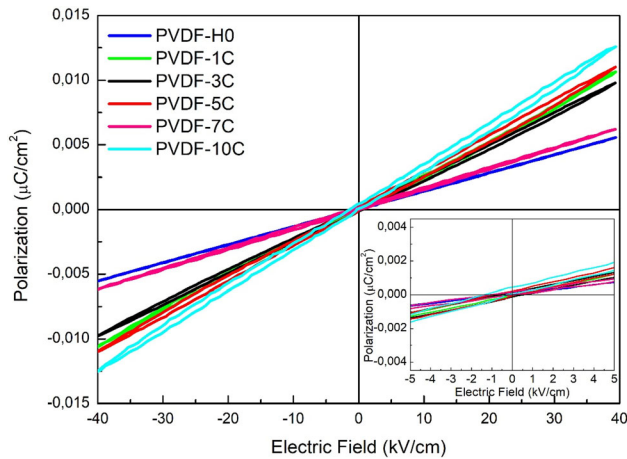


Fig. 7 P-E hysteresis loops of the pure PVDF and the PVDF/CFO nanofiber composites prepared with different levels of the CoFe_2O_4 content

The electrical performances of nanogenerators were calculated (Eq. 2), and compared according to the V_{RMS} values. As seen in Figs. 11 and 12, the maximum V_{RMS} values of 185.62 mV at 20 Hz and 130.34 mV at 10 Hz were found for the PVDF-5 C and the pure PVDF based nanogenerators, respectively.

When the performances of nanogenerators were compared to each other, the frequencies of 10 and 20 Hz were observed to be the reference resonant frequency values for the pure PVDF and the PVDF/CFO based nanogenerators, respectively (see Fig. 12).

The V_{RMS} changes exhibited by nanogenerators under resistive loads from 200 K Ω to 4 M Ω at vibrational frequencies of 10 Hz for the pure PVDF nanogenerators and 20 Hz for nanogenerators based on the PVDF/CFO are shown in Fig. 13. According to Fig. 13, the maximum voltage values at the same resistive load of 2.5 M Ω were obtained as 172.00 mV at 20 Hz for the PVDF-3 C and 152.30 mV at 10 Hz for the nanogenerator based on the pure PVDF (PVDF-H0).

The electrical power generated by the nanogenerator was calculated using the following equation,

$$P_{RMS} = \frac{(V_{L_{RMS}})^2}{RL} \quad (3)$$

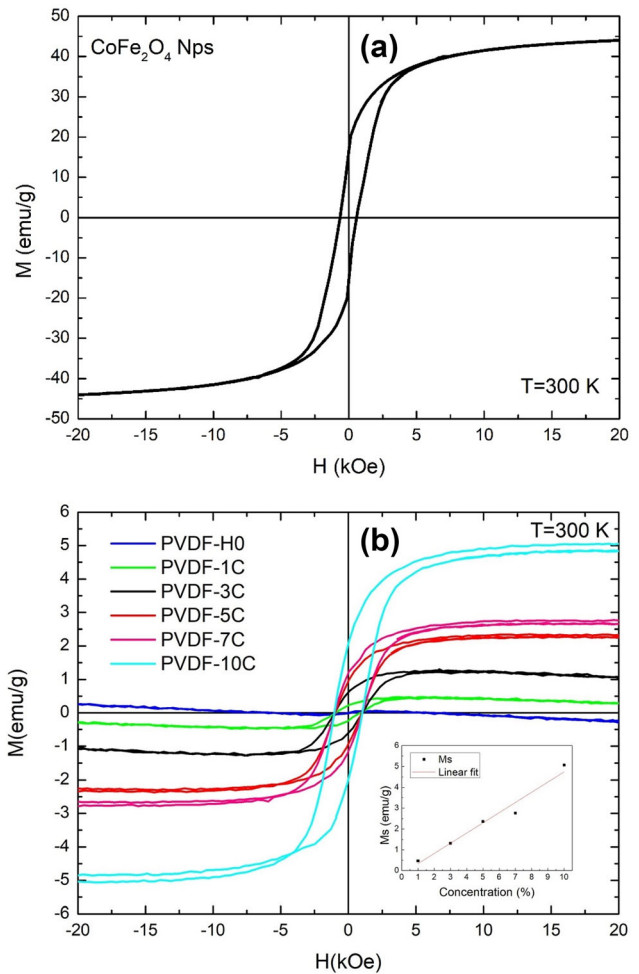


Fig. 8 Hysteresis loops of **a** CoFe_2O_4 NPs, **b** the pure PVDF and the PVDF/CFO nanocomposites at 300 K. The inset shows the M_s vs. concentration (%) of the CoFe_2O_4 NPs in the PVDF with linear fit (red line) (Color figure online)

where P_{RMS} and $V_{L_{RMS}}$ indicate the effective electrical power output of the nanogenerator and the effective voltage across the load of RL, respectively.

The electrical performances (V_{RMS} and P_{RMS}) of the PVDF-H0 (pure), the PVDF-3 C, and the PVDF-5 C are discussed in the results which are shown in Fig. 14. The highest electrical powers at the resistive load of 2.5 M Ω were in the amounts of 11.83 μW at 20 Hz for the nanogenerator based on the PVDF-3 C and 9.3 μW at 10 Hz for the pure PVDF based nanogenerator.

Another important parameter for the nanogenerator is its own capacitance value, which is defined by the following Eqs. [67],

$$V_{oc} = \frac{Q}{C} \quad (4)$$

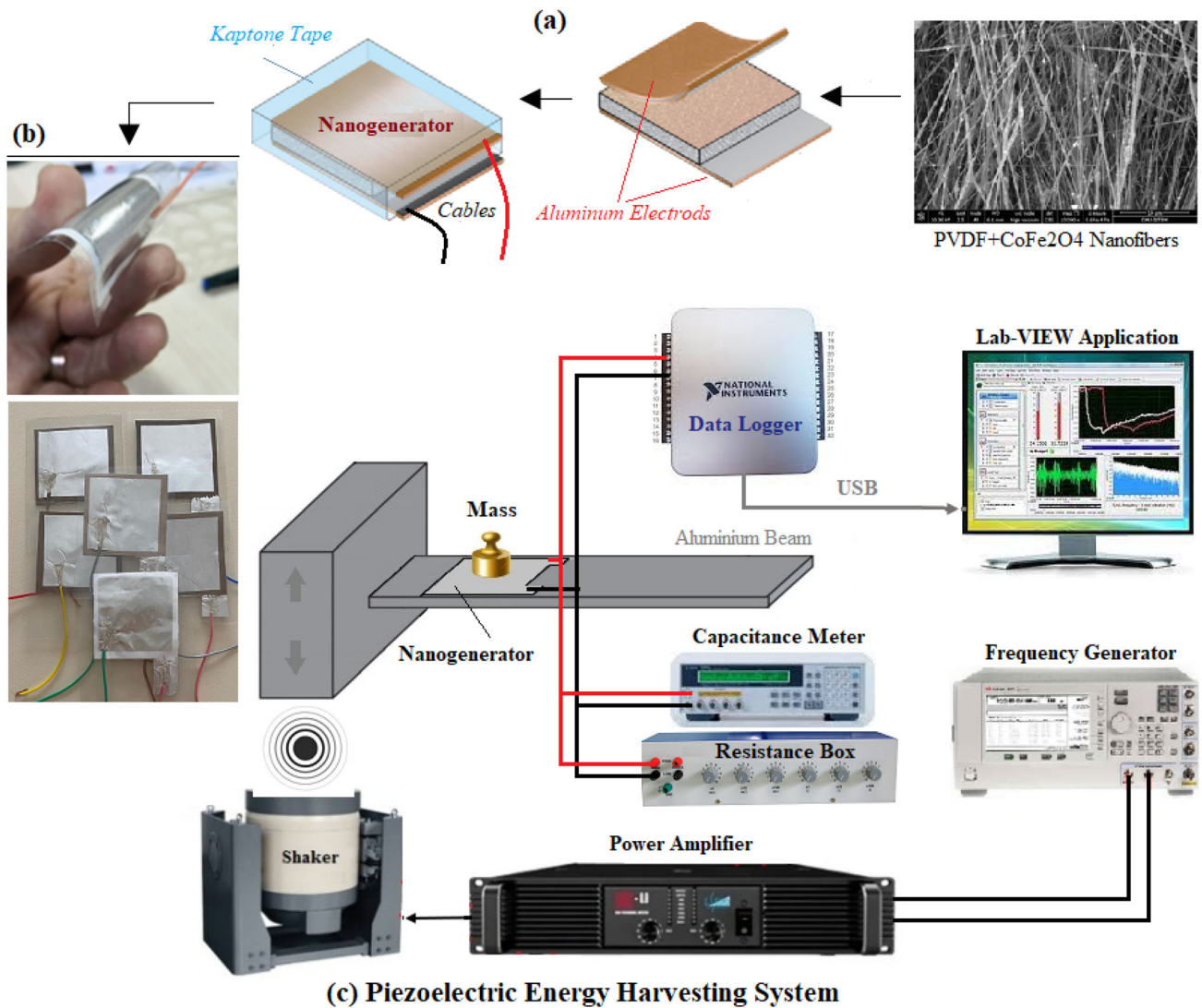


Fig. 9 Schematic fabrication steps of **a** the nanogenerator, **b** the real photos of flexible nanogenerators, and **c** Piezoelectric energy harvesting system with capacitance meter

where C , V_{oc} , and Q indicate the nanogenerator’s capacitance, the open-circuit voltage generated across the electrodes, and the accumulated charge on the nanogenerator induced by mechanical vibration, respectively.

Equation 4 shows the relationship between the charged induced on the nanogenerator, and the open-circuit voltage generated from it. Furthermore, in this study the capacitance measurements of the nanogenerators without resistive load were realized using a capacitance meter during the piezoelectric energy harvesting tests, and are presented in Fig. 15.

The highest capacity value was observed as 1.47 nF for the PVDF-5 C at 20 Hz during open-circuit voltage. There were very small differences between the measured capacitance values.

3.7.2 magnetoelectric effects on flexible nanogenerator

In order to evaluate the magnetoelectric effects on a flexible nanogenerator under a stray field environment, as shown in Fig. 16, the nanogenerator was mounted below the power cord of an electric kettle (220 V, 50 Hz, 1500 W) at a distance of 0.5 mm in order to create a maximum magnetic field [7].

The strength of magnetic field around the power cable depends on Ampere’s law as follows,

$$B = \frac{\mu_0 I}{2\pi d} \tag{5}$$

where B is the strength of the AC magnetic field, μ_0 is the magnetic constant ($4\pi \times 10^{-7} \text{Tm/A}$), I is the current drawn by the electrical kettle, and d is the distance between the power cable and the nanogenerator.

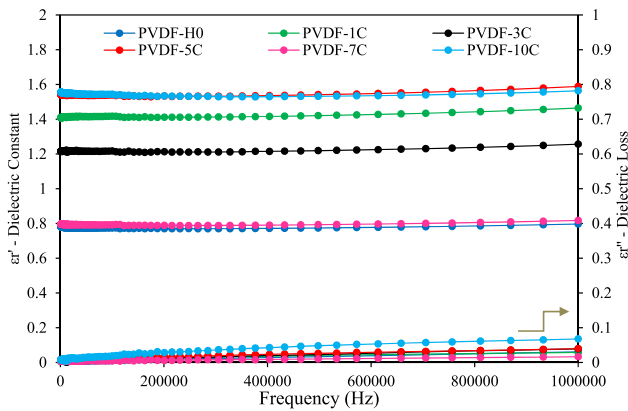


Fig. 10 Dielectric constant (ϵ_r') and dielectric loss (ϵ_r'') variations for the pure PVDF and the PVDF/COF nanocomposites at frequencies from 1 kHz to 1 MHz

In this study, the electric current induced on the nanogenerator through the power cable of the kettle was measured with load (in parallel) and without load by a data logger (NI-6009) including the LabVIEW software.

The AC sinusoidal electrical voltage changes (without load) induced on the nanogenerators with the PVDF-5 C, PVDF-7 C, and PVDF-10 C are indicated in Fig. 17. Although the pure PVDF composite is not expected to exhibit the magnetic properties, Fig. 17 shows that the addition of the CoFe_2O_4 NPs in the PVDF matrix contributed to harvesting voltages induced on the nanogenerator compared to the pure PVDF.

The V_{RMS} changes observed in the nanogenerators based on the PVDF-5 C, the PVDF-7 C, and the PVDF-10 C are shown in Fig. 18. Accordingly, the PVDF-10 C reached the highest voltage value of 18.87 mV under a resistive load of 2.5 $\text{M}\Omega$.

4 Conclusion

Flexible pure PVDF and the PVDF/ CoFe_2O_4 based nanogenerators were successfully fabricated through electrospinning system equipped with a rotating

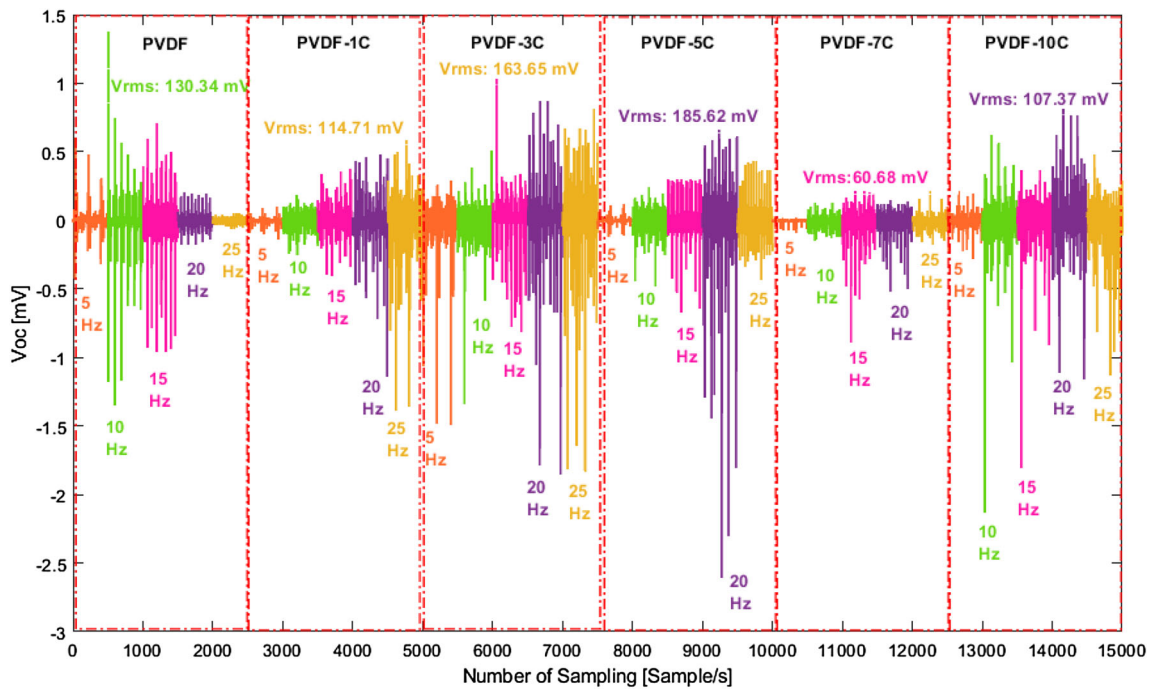


Fig. 11 The V_{OC} (V_{pp}) and V_{RMS} changes of the pure PVDF and the PVDF/COF based nanogenerators

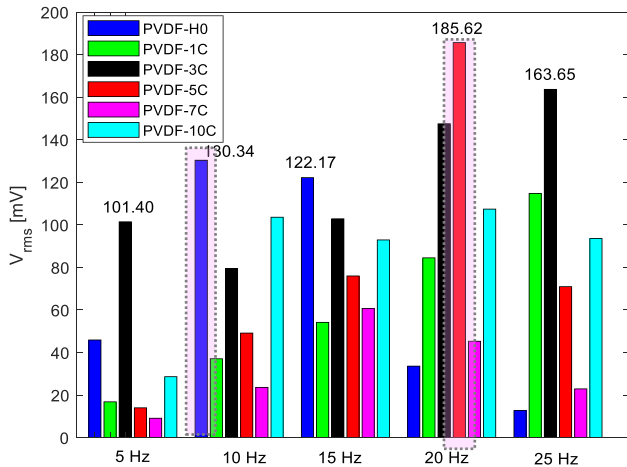


Fig. 12 The V_{RMS} changes of nanogenerators according to various vibration frequencies

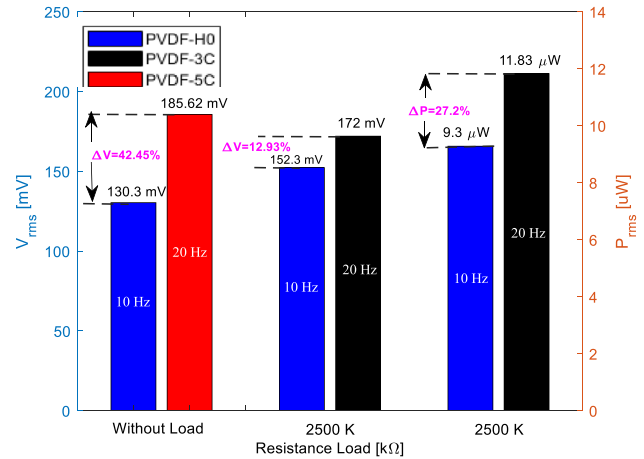


Fig. 14 Performance comparisons in V_{RMS} and P_{RMS} for the pure PVDF (10 Hz) and the PVDF/CFO (20 Hz) under non-resistive loads and a 2.5 M Ω resistive load

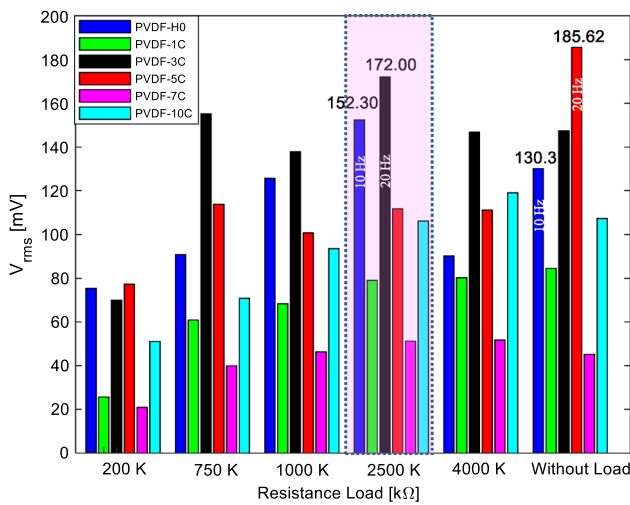


Fig. 13 The V_{RMS} versus resistance loads at vibrational frequencies of 10 Hz for the pure PVDF nanogenerator and 20 Hz for nanogenerators based on the PVDF/CFO

drum collector. The addition of the different weight rates of the $CoFe_2O_4$ NPs content into the PVDF induces the PVDF's ferroelectric crystalline β phase. Among all PVDF/ $CoFe_2O_4$ samples, the PVDF/ $CoFe_2O_4$ fibers containing the $CoFe_2O_4$ NPs at a concentration of 5 wt% achieve a better crystalline β phase which is higher than the pure PVDF. According to the FTIR and SEM analyses, the aligned pure PVDF and the PVDF/ $CoFe_2O_4$ fibers were observed to have a rich β -phase content in the average diameters of 180–912 nm. The variation of the ferroelectric characteristics according to the magnetic field reveals the magnetoelectric properties and the cross coupling

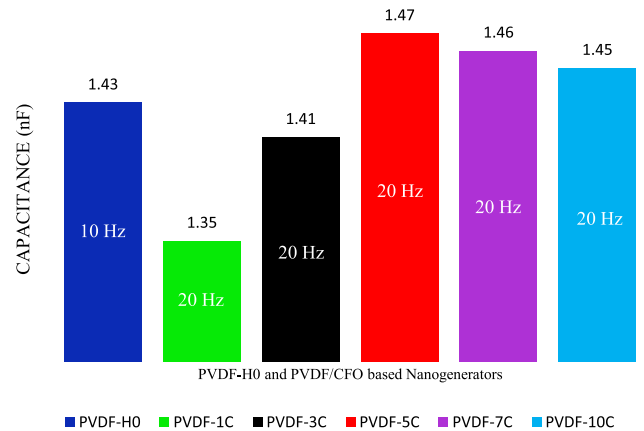


Fig. 15 The capacitance changes of nanogenerators during the piezoelectric energy harvesting tests without load

between the ferroelectric and ferromagnetic ordering. The piezoelectric performances of the nanogenerators were investigated under various resistive loads from 200K Ω to 4M Ω in parallel with the piezoelectric energy harvesting system. The experimental results showed that the maximum output power of the nanogenerator with 3 wt% $CoFe_2O_4$ NPs reaches 11.83 μW at 20 Hz excitation frequency by increasing the power to 27.2% under a resistive load of 2.5M Ω , while the nanogenerator with the pure PVDF has an electrical power of 9.3 μW at 10 Hz excitation frequency under the same load. It was concluded that the incorporation of the $CoFe_2O_4$ NPs into the polymer matrix not only increased the electrical power but also shifted the resonance detection frequency from 10 to 20 Hz compared to the nanogenerator based on the pure PVDF as well.

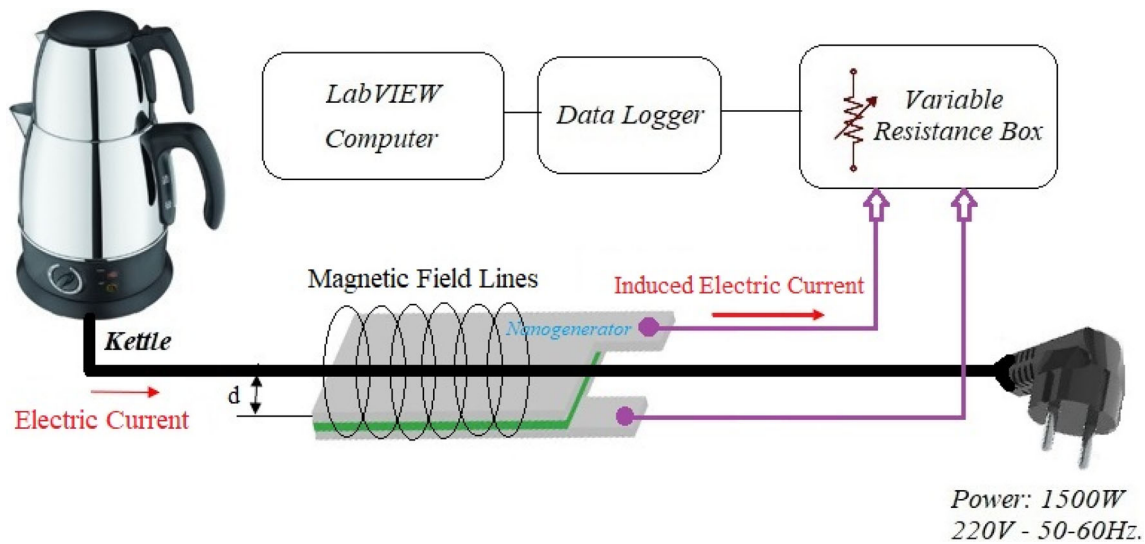


Fig. 16 The schematic of the energy harvesting system based on the magnetic field

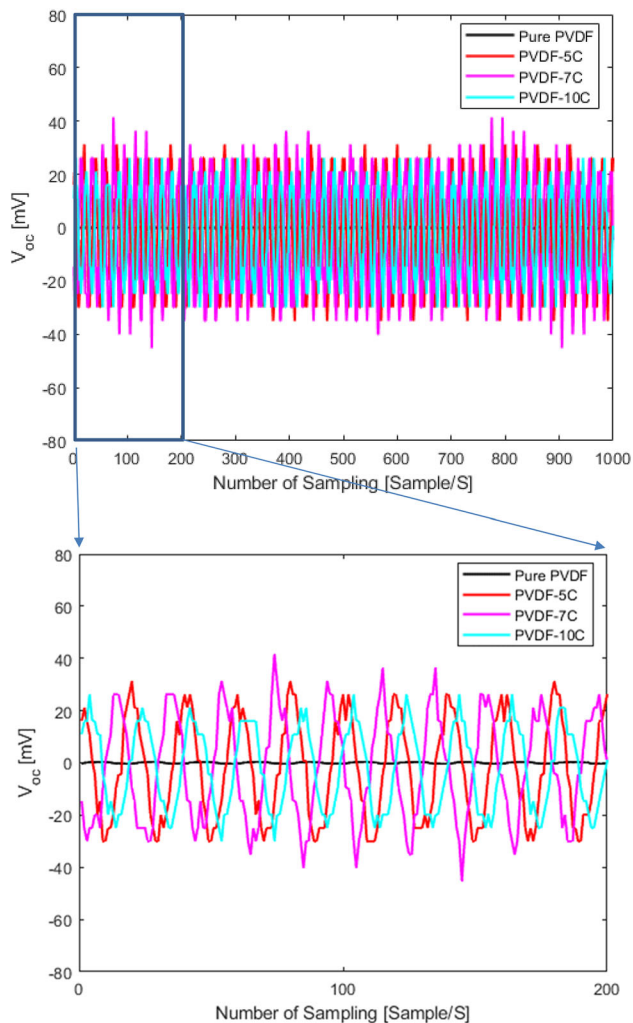


Fig. 17 Comparison of harvesting voltages induced on nanogenerator through the power cable of an electric kettle

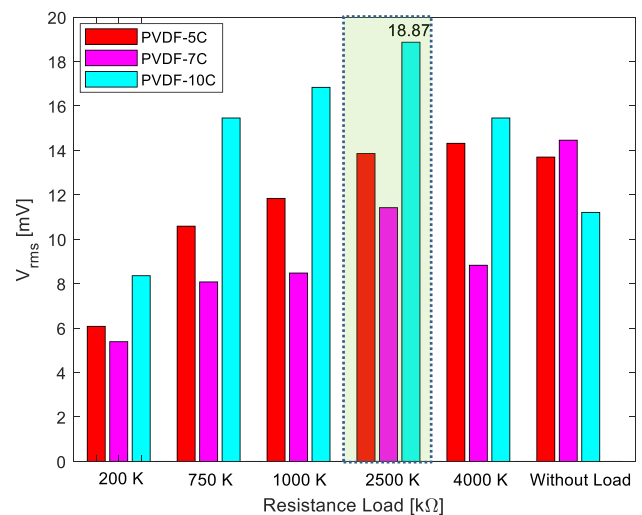


Fig. 18 The V_{RMS} changes observed of nanogenerators based the PVDF-5 C, the PVDF-7 C, and the PVDF-10 C

In order to define the ME properties of the nanogenerators, the magnetic field associated with an electrical kettle power cord was used. The nanogenerator based on the PVDF/ CoFe_2O_4 fibers containing CoFe_2O_4 NPs at a concentration of 10 wt% reached the highest voltage of 18.87 mV under a resistive load of 2.5MΩ at a low-level magnetic field frequency of 50 Hz. Such flexible PVDF/ CoFe_2O_4 fiber mats with multifunctional properties can contribute to the development of some equipment such as actuators, sensors, and memory devices.

Author contribution

MK: fabrications of the nanofiber composites, and their morphology analyzes. ÇEDD: Synthesis of the powder material with nano-size, and magnetic analyzes of the nanofiber composites. LP: Conception and design of the study, interpretation of all data, drafting the manuscript. AS: Acquisition of data from measurements related to energy harvesting applications. SA: Interpretation of magnetic properties on powder material. Revising the manuscript critically for important intellectual content.

Data Availability

The authors confirm that the data supporting the finding of this study are available within the article. Raw data that support the findings of this study are available from the corresponding author upon reasonable request.

Declarations

Conflict of interest The authors declare that they have no known competing financial interests or personal relationships that could have appeared to influence the work reported in this paper.

References

1. S. Priya, *J Electroceram.* **19**, 165 (2007)
2. F.K. Shaikh, S. Zeadally, *Renew. Sustain. Energy Rev.* **55**, 1041 (2016)
3. R.L. Harné, K.W. Wang, *Smart Mater. Struct.* **22**, 023001 (2013)
4. A.R.M. Siddique, S. Mahmud, B. Van Heyst, *Energy Convers. Manag.* **106**, 728 (2015)
5. J. Zhang, C. Wang, C. Bowen, *Nanoscale* **6**, 13314 (2014)
6. J. Ryu, J.E. Kang, Y. Zhou, S.Y. Choi, W.H. Yoon, D.S. Park, J.J. Choi, B.D. Hahn, C.W. Ahn, J.W. Kim, Y. Do Kim, S. Priya, S.Y. Lee, S. Jeong, D.Y. Jeong, *Energy Environ. Sci.* **8**, 2402 (2015)
7. S.K. Ghosh, K. Roy, H.K. Mishra, M.R. Sahoo, B. Mahanty, P.N. Vishwakarma, D. Mandal, *ACS Sustain. Chem. Eng.* **8**, 864 (2020)
8. Y. Uzun, E. Kurt, *Energy Convers. Manag.* **72**, 156 (2013)
9. N.A. Spaldin, R. Ramesh, *Nat. Mater.* **18**, 203 (2019)
10. D.K. Pradhan, A.K. Mishra, S. Kumari, A. Basu, M. Somayazulu, E. Gradauskaite, R.M. Smith, J. Gardner, P.W. Turner, A.T. N'Diaye, M.B. Holcomb, R.S. Katiyar, P. Zhou, G. Srinivasan, J.M. Gregg, J.F. Scott, *Sci. Rep.* **9**, 1 (2019)
11. A.S. Fawzi, A.D. Sheikh, V.L. Mathe, *J. Alloys Compd.* **493**, 601 (2010)
12. C.W. Nan, M.I. Bichurin, S. Dong, D. Viehland, G. Srinivasan, *J. Appl. Phys.* **103**(3), 1 (2008)
13. D.S. Jeong, R. Thomas, R.S. Katiyar, J.F. Scott, H. Kohlstedt, A. Petraru, C.S. Hwang, *Reports. Prog. Phys.* **750**, 0765 (2012)
14. M. Bibes, A. Barthélémy, *Nat. Mater.* **7**, 425 (2008)
15. J.F. Scott, *Nat. Mater.* **6**, 256 (2007)
16. D.K. Pradhan, S. Kumari, P.D. Rack, *Nanomaterials* **10**, 1 (2020)
17. S.K. Chacko, M.T. Rahul, B. Raneesh, N. Kalarikkal, *New. J. Chem.* **44**, 11356 (2020)
18. V. Annapureddy, H. Palneedi, G.T. Hwang, M. Peddigari, D.Y. Jeong, W.H. Yoon, K.H. Kim, J. Ryu, *Sustain. Energy Fuels* **1**, 2039 (2017)
19. Y. Wang, J. Hu, Y. Lin, C.W. Nan, *NPG Asia Mater.* **2**, 61 (2010)
20. M. Ben Ali, K. El Maalam, H. El Moussaoui, O. Mounkachi, M. Hamedoun, R. Masrour, E.K. Hlil, A. Benyoussef, *J. Magn. Magn. Mater.* **398**, 20 (2016)
21. V. Madhav Kumar, A. Srinivas, A. Talapatra, S. Asthana, J. Mohanty, S.V. Kamat, *J. Mater. Sci. Mater. Electron.* **28**, 446 (2017)
22. N. Quandt, R. Roth, F. Syrowatka, M. Steimecke, S.G. Ebbinghaus, *J. Solid State Chem.* **233**, 82 (2016)
23. P. Martins, A. Lasheras, J. Gutierrez, J.M. Barandiaran, I. Orue, S. Lanceros-Mendez, *J. Phys. D. Appl. Phys.* **44**, 495303 (2011)
24. P.D. Prasad, J. Hemalatha, *Mater. Res. Express* **6**(9), 094007 (2019)
25. A.C. Lima, N. Pereira, P. Martins, S. Lanceros-Mendez, *Handb. Magn. Mater.* **29**, 57 (2020)
26. B. Ameduri, *Chem. Rev.* **109**, 6632 (2009)
27. P. Martins, A.C. Lopes, S. Lanceros-Mendez, *Prog Polym. Sci.* **39**, 683 (2014)
28. T. Prabhakaran, J. Hemalatha, Wiley-VCH Verlag GmbH & Co. KGaA. (2017)
29. Y. Slimani, S.E. Shirsath, E. Hannachi, M.A. Almessiere, M.M. Aouna, N.E. Aldossary, G. Yasin, A. Baykal, B. Özçelik, I. Ercan, *J. Am. Ceram. Soc.* **104**, 5648 (2021)
30. Y. Slimani, M.A. Almessiere, S.E. Shirsath, E. Hannachi, G. Yasin, A. Baykal, B. Özçelik, I. Ercan, *J. Magn. Magn. Mater.* **510**, (2020)
31. D. Kim, M.D. Rossell, M. Campanini, R. Erni, J. Puigmartí-Luis, X.Z. Chen, S. Pané, *Appl. Phys. Lett.* **119**, 0 (2021)

32. C.E. Ciomaga, A. Guzu, M. Airimioaei, L.P. Curecheriu, V.A. Lukacs, O.G. Avadanei, G. Stoian, M. Grigoras, N. Lupu, M. Asandulesa, L. Mitoseriu, *Ceram. Int.* **45**, 24168 (2019)
33. A. Guzu, C.E. Ciomaga, M. Airimioaei, L. Padurariu, L.P. Curecheriu, I. Dumitru, F. Gheorghiu, G. Stoian, M. Grigoras, N. Lupu, M. Asandulesa, L. Mitoseriu, *J. Alloys Compd.* **796**, 55 (2019)
34. P. Durgaprasad, J. Hemalatha, *J. Magn. Magn. Mater.* **448**, 94 (2018)
35. P. Martins, C.M. Costa, M. Benelmekki, S. Lanceros-Mendez, *Sens. Lett.* **11**, 110 (2013)
36. T. Zheng, Z. Yue, G.G. Wallace, Y. Du, P. Martins, 065707, (n.d.)
37. K. Maaz, A. Mumtaz, S.K. Hasanain, A. Ceylan, *J. Magn. Magn. Mater.* **308**, 289 (2007)
38. M. Koç, L. Paralı, O. Şan, *Polym. Test.* **90**, (2020)
39. C.M. Wu, M.H. Chou, W.Y. Zeng, *Nanomaterials* **8**, 1 (2018)
40. J. Rodríguez-carvajal, L.L.B. Cea-cnrs, C.E.A. Saclay, Y. Cedex, *Cogn. Ther. Groups 1* (2008)
41. J. Rodríguez-Carvajal, *Phys. B Phys. Condens. Matter* **192**, 55 (1993)
42. C. Dey, K. Baishya, A. Ghosh, M.M. Goswami, A. Ghosh, K. Mandal, *J. Magn. Magn. Mater.* **427**, 168 (2017)
43. E. Darezereshki, M. Ranjbar, F. Bakhtiari, *J. Alloys Compd.* **502**, 257 (2010)
44. P.D. Prasad, J. Hemalatha, *J. Magn. Magn. Mater.* **532**, 167986 (2021)
45. M. Sang, S. Wang, M. Liu, L. Bai, W. Jiang, S. Xuan, X. Gong, *Compos. Sci. Technol.* **165**, 31 (2018)
46. T. Lei, X. Cai, X. Wang, L. Yu, X. Hu, G. Zheng, W. Lv, L. Wang, D. Wu, D. Sun, L. Lin, *RSC Adv.* **3**, 24952 (2013)
47. R. Gregorio, M. Cestari, *J. Polym. Sci. Part. B Polym. Phys.* **32**, 859 (1994)
48. X. Cai, T. Lei, D. Sun, L. Lin, *RSC Adv.* **7**, 15382 (2017)
49. L. Li, M. Zhang, M. Rong, W. Ruan, *RSC Adv.* **4**, 3938 (2014)
50. R. K, G.P. Kar, S. Bose, B. Basu, *RSC Adv.* **6**, 10837 (2016)
51. Y. Peng, P. Wu, *Polym. (Guildf)* **45**, 5295 (2004)
52. Y. Xin, X. Qi, H. Tian, C. Guo, X. Li, J. Lin, C. Wang, *Mater. Lett.* **164**, 136 (2016)
53. S. Janakiraman, A. Surendran, S. Ghosh, S. Anandhan, A. Venimadhav, *Solid State Ionics* **292**, 130 (2016)
54. N. Chakhchaoui, R. Farhan, A. Eddiai, M. Meddad, O. Cherkaoui, M. Mazroui, Y. Boughaleb, L. van Langenhove, *Mater. Today Proc.* **39**, 1148 (2019)
55. S. Yoon, A.A. Prabu, K.J. Kim, C. Park, *Macromol. Rapid Commun.* **29**, 1316 (2008)
56. C.L. Liang, Z.H. Mai, Q. Xie, R.Y. Bao, W. Yang, B.H. Xie, M.B. Yang, *J. Phys. Chem. B* **118**, 9104 (2014)
57. P. Zhang, X. Zhao, X. Zhang, Y. Lai, X. Wang, J. Li, G. Wei, Z. Su, *ACS Appl. Mater. Interfaces* **6**, 7563 (2014)
58. W. Zhou, X. Jiang, P. Wang, H. Wang, *Fibers Polym.* **14**, 100 (2013)
59. Y. Ji, B. Li, S. Ge, J.C. Sokolov, M.H. Rafailovich, *Langmuir* **22**, 1321 (2006)
60. S. Garain, S. Jana, T.K. Sinha, D. Mandal, *ACS Appl. Mater. Interfaces* **8**, 4532 (2016)
61. R.H. Kodama, A.E. Berkowitz, E.J. McNiff, S. Foner, *Mater. Sci. Forum* **235–238**, 643 (1997)
62. I.J. Bruvera, P. Mendoza Zélis, M. Pilar Calatayud, G.F. Goya, F.H. Sánchez, *J. Appl. Phys.* **118**(18), 430 (2015)
63. M. Létiche, E. Eustache, J. Freixas, A. Demortière, V. De Andrade, L. Morgenroth, P. Tilmant, F. Vaurette, D. Troadec, P. Roussel, T. Brousse, C. Lethien, *Adv. Energy Mater.* **7**, 1 (2017)
64. L.C. Haspert, S.B. Lee, G.W. Rubloff, *ACS Nano* **6**, 3528 (2012)
65. J. Zhao, Z. You, *Sens. (Switzerland)* **14**, 12497 (2014)
66. V.N. Mittle, A. Mittal, *Basic Electrical Engineering*, 2nd edn. (McGraw-Hill, New Delhi, 2006)
67. M.A. Ilyas, *Piezoelectric Energy Harvesting, Methods, Progress, and Challenges* (Momentum Press, New York, 2018)

Publisher's Note Springer Nature remains neutral with regard to jurisdictional claims in published maps and institutional affiliations.